

OFDM-Based ISAC Imaging of Extended Targets via Inverse Virtual Aperture Processing

Michael Negosanti, Lorenzo Pucci, and Andrea Giorgetti

Abstract—This work investigates the performance of an integrated sensing and communication (ISAC) system exploiting inverse virtual aperture (IVA) for imaging moving extended targets in vehicular scenarios. A base station (BS) operates as a monostatic sensor using MIMO-OFDM waveforms. Echoes reflected by the target are processed through motion-compensation techniques to form an IVA range–Doppler (cross-range) image. A case study considers a 5G NR waveform in the upper mid-band, with the target model defined in 3GPP Release 19, representing a vehicle as a set of spatially distributed scatterers. Performance is evaluated in terms of image contrast (IC) and the root mean squared error (RMSE) of the estimated target-centroid range. Finally, the trade-off between sensing accuracy and communication efficiency is examined by varying the subcarrier allocation for IVA imaging. The results provide insights for designing effective sensing strategies in next-generation radio networks.

I. INTRODUCTION

THE integrated sensing and communication (ISAC) paradigm is widely recognized as one of the key pillars of next-generation 6G networks, enabling future systems to move beyond traditional communication services and provide ubiquitous sensing capabilities. Within the 6G vision, such native sensing is expected to support a wide range of applications, including assisted navigation, activity recognition, motion tracking, environmental monitoring, and imaging of objects and their surroundings. Among the sensing methods best suited to these applications, particularly for autonomous driving, which requires operation under all weather conditions and high-resolution mapping, virtual-aperture-based techniques are especially promising [1]–[3].

In this context, the sensing capabilities of orthogonal frequency division multiplexing (OFDM) waveforms can also be leveraged for radio imaging applications based on virtual aperture (VA) or inverse virtual aperture (IVA) techniques [4]–[6]. In particular, IVA stands out as one of the most suitable technologies, as it enables the imaging of non-cooperative targets even when the sensing base station (BS) remains stationary [7]. To the best of the authors' knowledge, the existing literature still lacks studies analyzing an OFDM-based ISAC–IVA system in a 3D scenario, aimed at assessing its performance and the impact of resource allocation between imaging and communication.

This work was supported, in part, by the CNIT National Laboratory WiLab and the WiLab-Huawei Joint Innovation Center, and in part by the European Union under the Italian National Recovery and Resilience Plan (NRRP) of NextGenerationEU, partnership on “Telecommunications of the Future” (PE00000001 - program “RESTART”).

The authors are with the Dept. of Electrical, Electronic, and Inf. Eng. “Guglielmo Marconi,” University of Bologna, and CNIT/WiLab, Italy (e-mail: {michael.negosanti2, lorenzo.pucci3, andrea.giorgetti}@unibo.it).

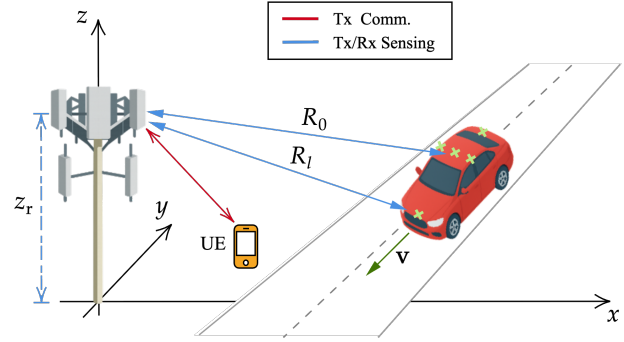


Fig. 1. Schematic representation of an ISAC–IVA setup with a BS using part of the physical-layer resources to perform imaging of a moving vehicle.

This study investigates the use of IVA imaging in multiple-input multiple-output (MIMO)–OFDM systems, such as 5G and 6G, where the sensing BS operates in a monostatic configuration. The objective is to assess the performance of IVA-based methods in terms of image contrast and target-centroid estimation accuracy as a function of the sensing resources allocated. In particular: *i*) We design an IVA-based imaging system at the BS, leveraging MIMO–OFDM waveforms in a monostatic configuration. *ii*) We adopt the extended-target model recently standardized in 3GPP Release 19 to represent a vehicle. *iii*) We apply motion-compensation techniques to generate an IVA range–Doppler image, which is then post-processed through thresholding to estimate the target-centroid range. *iv*) We analyze how the fraction of subcarriers allocated to sensing affects both the root mean squared error (RMSE) of the target-centroid range estimate and the image contrast (IC) metric, considering a case study based on 5G NR operation in the upper mid-band.

Throughout the paper, capital boldface letters denote matrices; lowercase boldface letters denote vectors; $(\cdot)^T$, $(\cdot)^H$, $\lceil \cdot \rceil$, $\|\cdot\|$, and $\|\cdot\|_F$ represent transpose, conjugate transpose, ceiling function, Euclidean, and Frobenius norms, respectively; $\mathbf{X}_{:,n}$ is the n th column of \mathbf{X} ; $\mathbf{1}_{M \times N}$ and $\mathbf{1}_N$ are all-one matrix and vector, respectively; $\mathbb{E}\{\cdot\}$ denotes expectation; $\mathbf{x} \sim \mathcal{CN}(\mathbf{0}, \mathbf{\Sigma})$ indicates a zero-mean circularly symmetric complex Gaussian vector with covariance $\mathbf{\Sigma}$; $\text{FFT}_N\{\cdot\}$ denotes an N -point fast Fourier transform (FFT).

II. SYSTEM MODEL

We consider a monostatic MIMO-OFDM BS as shown in Fig. 1, that communicates with user equipments (UEs), while

simultaneously processing echoes generated by a moving vehicle to produce IVA images. The BS is equipped with a transmit uniform linear array (ULA) with N_T antennas for downlink transmission and a separate receive ULA with N_R elements for backscattered signal collection, both horizontally aligned along the y -axis of Fig. 1. For both the ULAs, we consider an inter-element spacing $d = \lambda/2$, where $\lambda = c/f_c$, with c the speed of light and f_c the carrier frequency.

A. Transmit signal

The ISAC system transmits OFDM frames composed of M OFDM symbols in the time domain and K active subcarriers. Given a subcarrier spacing $\Delta f = 1/T$, where T denotes the OFDM symbol duration (without the cyclic prefix), the total signal bandwidth is $B = K\Delta f$. The total frame duration is $T_f = MT_s$, where $T_s = T + T_g$ is the total OFDM symbol duration including the cyclic prefix (CP) of duration T_g , introduced to avoid intersymbol interference (ISI). For each frame, a portion of the time-frequency resources is allocated to sensing (imaging) operations, with a sensing repetition interval (SRI), i.e., the time between two consecutive sensing symbols, equal to $T_{\text{SRI}} = N_s T_s$, where $N_s \in \mathbb{N}$, and a sensing bandwidth $B_s = K_s \Delta f$. To illuminate the entire spatial extent of a moving target, M_s sensing OFDM symbols are considered over multiple consecutive frames, leading to a total coherent processing interval (CPI) of $T_{\text{CPI}} = M_s T_{\text{SRI}} > T_f$.

Hereinafter, we indicate with $\rho_f = K_s/K$ and $\rho_t = \frac{T_s \lceil M/N_s \rceil}{T_f}$ the fraction of subcarriers and fraction of frame time allocated to sensing, respectively.

For each OFDM frame, a time-frequency grid \mathbf{X} of complex modulation symbols $x_{k,m}$ is considered, where each symbol corresponds to subcarrier index $k = 0, \dots, K-1$ and time index $m = 0, \dots, M-1$, and is normalized such that $\mathbb{E}\{|x_{k,m}|^2\} = 1$. Prior to transmission, the symbols are precoded across the N_T transmit antennas by means of a digital beamforming vector $\mathbf{w}_T \in \mathbb{C}^{N_T \times 1}$, which depends on the system operation mode, i.e., sensing or communication. This work focuses on the sensing operation, where the goal is to perform moving-target imaging via IVA processing. Therefore, details related to communication beamforming are omitted.

For imaging applications, \mathbf{w}_T is designed to generate a wide sensing beam, with beamwidth $\Delta\Theta_T$, to cover the target trajectory during a CPI, following the approach in [8]. Although this design entails a reduction in beamforming gain compared to a narrow beam, it ensures that the entire spatial extent of the target is illuminated with approximately constant gain and phase.¹ Preserving phase coherence during target motion is essential for accurate inverse aperture synthesis and high-fidelity image reconstruction. The beamforming vector is normalized as $\|\mathbf{w}_T\|^2 = P_{\text{avg}}$, where $P_{\text{avg}} = P_T/K$ denotes the average transmit power per subcarrier, given a total

¹Each wide beam is, in principle, designed to illuminate a single target along its trajectory. In the presence of multiple targets, they can be sequentially illuminated, e.g., in a time-division manner.

transmit power P_T . After beamforming, the $[N_T \times 1]$ vector of complex transmit symbols $\mathbf{x}[k, m] = x_{k,m} \mathbf{w}_T$ is obtained for each subcarrier k and OFDM symbol m . Hereinafter, the index $m_s \in \{0, \dots, M_s-1\}$ is introduced to indicate sensing OFDM symbols extracted from the transmitted grids over multiple consecutive frames with a sampling interval T_{SRI} .

B. Sensing signal received

At the sensing receiver, echoes reflected by surrounding targets are collected. After demodulation through the FFT, the sensing receiver extracts the symbols over the K_s contiguous subcarriers every T_{SRI} for further processing. For subcarrier k and sensing time index m_s , the complex received signal vector of size $[N_R \times 1]$, under the assumption of negligible ISI and intercarrier interference (ICI), is expressed as²

$$\mathbf{y}[k, m_s] = \mathbf{H}[k, m_s] \mathbf{x}[k, m_s] + \mathbf{n}[k, m_s] \quad (1)$$

where $\mathbf{H}[k, m_s] \in \mathbb{C}^{N_R \times N_T}$ denotes the MIMO channel matrix containing information related to the targets, and $\mathbf{n}[k, m_s] \sim \mathcal{CN}(0, \sigma^2 \mathbf{I}_{N_R})$ represents the noise, assumed independent, identically distributed (i.i.d.) across subcarriers and time. The noise variance is $\sigma^2 = N_0 \Delta f$, with N_0 the one-sided noise power spectral density (PSD).

We consider line-of-sight (LoS) propagation and a single extended target composed of L scattering points. For a given scatterer l , the round-trip delay, azimuthal angle of arrival (AoA)/angle of departure (AoD), and complex channel gain sampled at time $m_s T_{\text{SRI}}$ are denoted by $\tau_l[m_s] \triangleq \tau_l(m_s T_{\text{SRI}})$, $\theta_l[m_s] \triangleq \theta_l(m_s T_{\text{SRI}})$, and $\alpha_l[m_s] \triangleq \alpha_l(m_s T_{\text{SRI}})$, respectively. These parameters are assumed constant within each OFDM symbol (fast time) but may vary across sensing symbols (slow time) due to target motion. Under these assumptions, the channel matrix in (1) can be written as

$$\mathbf{H}[k, m_s] = \sum_{l=1}^L \underbrace{\alpha_l[m_s] e^{-i4\pi k \Delta f \frac{R_l[m_s]}{c}}}_{\triangleq \beta_l[m_s]} \mathbf{a}_R(\theta_l[m_s]) \mathbf{a}_T^H(\theta_l[m_s]) \quad (2)$$

where $R_l[m_s]$ denotes the distance between scatterer l and the BS at time m_s while $\mathbf{a}_R(\cdot)$ and $\mathbf{a}_T(\cdot)$ represent the receive and transmit array response vectors, respectively. The transmit array response is defined as [9]³

$$\mathbf{a}_T(\theta_l[m_s]) = [e^{-i\frac{N_T-1}{2}\pi \sin(\theta_l[m_s])}, \dots, e^{i\frac{N_T-1}{2}\pi \sin(\theta_l[m_s])}]^T. \quad (3)$$

The same definition applies to $\mathbf{a}_R(\theta_l[m_s])$ with N_R elements.

The complex channel gain models attenuation and phase shift along the l th path at time m_s and is given by $\alpha_l[m_s] = \tilde{\alpha}_l[m_s] e^{i\tau_l[m_s]}$. According to the radar equation, we define the channel gain as $\tilde{\alpha}_l[m_s] = \sqrt{\frac{G_T G_R \sigma_l c^2}{(4\pi)^3 f_c^2 R_l^4[m_s]}}$, where G_T and G_R represent the single transmit and receive antenna gains, and

²Note that monostatic sensing requires a full-duplex architecture with self interference (SI) cancellation. In this work, we consider the residual SI after cancellation to be negligible with respect to Gaussian noise.

³Since the considered ULAs scan only the azimuth plane and the target elevation angle varies slightly during its motion, elevation effects are negligible and thus omitted from the array model.

σ_l is the radar cross-section (RCS) of the l th scatterer [10]. The phase is given by $\gamma_l[m_s] = -4\pi f_c \frac{R_l[m_s]}{c} + \phi_l$, where the former term is a deterministic component due to the round-trip propagation delay, while $\phi_l \sim \mathcal{U}(0, 2\pi)$ is a random scattering phase, representing the residual phase offset associated with the small-scale structure of the scatterer, assumed constant over the CPI.

Beamforming is then applied to the received symbol vector in (1) by using the receive weight vector $\mathbf{w}_R \in \mathbb{C}^{N_R \times 1}$ to obtain the received symbol y_{k,m_s} . The beamforming vector \mathbf{w}_R is assumed to be designed the same way as \mathbf{w}_T , i.e., to produce a wide beam, with beamwidth $\Delta\Theta_R$, centered at a given sensing azimuthal direction θ_s , with $\|\mathbf{w}_R\|^2 = 1$ (see Section II-A). Considering (1), and plugging into it the channel matrix in (2), the resulting received symbol becomes

$$y_{k,m_s} = \left(\sum_{l=1}^L \beta_l[m_s] \Upsilon(\theta_l[m_s], \theta_s) \right) x_{k,m_s} + \tilde{n}_{k,m_s} \quad (4)$$

where $\tilde{n}_{k,m_s} = \mathbf{w}_R^H \mathbf{n}_{k,m_s} \sim \mathcal{CN}(0, \sigma^2)$ is the noise after beamforming, and $\Upsilon(\theta_l[m_s], \theta_s) \in \mathbb{C}$ is the composite transmitting-receiving beamforming gain along the azimuthal direction $\theta_l[m_s]$ at time m_s . Moreover, $\beta_l[m_s]$, defined in (2), contains information about the range and Doppler of scatterer l at time m_s . From (4), we remove the transmitted data symbol x_{k,m_s} , which represents a nuisance parameter, by element-wise reciprocal filtering [11]. This operation is repeated for each (k, m_s) pair to produce the sensing data matrix $\mathbf{G}_s \in \mathbb{C}^{K_s \times M_s}$, which is subsequently used to reconstruct an IVA range-Doppler (or range-cross-range) image. In particular, the (k, m_s) entry of \mathbf{G}_s is

$$g_{k,m_s} = \frac{y_{k,m_s}}{x_{k,m_s}} = \sum_{l=1}^L \beta_l[m_s] \Upsilon(\theta_l[m_s], \theta_s) + \nu_{k,m_s} \quad (5)$$

where $\nu_{k,m_s} = \tilde{n}_{k,m_s}/x_{k,m_s} \sim \mathcal{CN}\left(0, \sigma^2 \mathbb{E}\left\{1/|x_{k,m_s}|^2\right\}\right)$.⁴

C. Range and Doppler reconstruction

As shown in Fig. 1, we consider a vehicular target moving with uniform rectilinear motion at a constant speed $v = |\mathbf{v}|$, where \mathbf{v} denotes the velocity vector. The target's motion alters its aspect angle as observed by the sensing system. This variation in viewing angle results in an apparent rotation of the target, which is effectively equivalent to a true rotational motion from an imaging perspective. The resulting apparent rotation induces spatially dependent Doppler frequency shifts that can be exploited to discriminate scatterers located at different spatial positions [7].

Let R_0 denote the initial reference range between the center of the extended target and the BS, and let (x, y, z) and (x', y', z') represent the global (space-fixed) and local (target-fixed) Cartesian coordinate systems, respectively. The space-fixed frame is centered at the BS position with zero rotation

⁴When a constant-envelope modulation is used (e.g., quadrature phase shift keying (QPSK)), $|x_{k,m_s}|^2 = 1$ for all k, m_s , hence $\mathbb{E}\left\{1/|x_{k,m_s}|^2\right\} = 1$. Otherwise, the noise variance increases after element-wise division (see [12]).

angle, whereas the target-fixed frame has its origin at the target center. Assuming that the BS-to-target distance is much larger than the physical dimensions of the target, which is commonly referred to as the straight iso-range approximation [13], the 3D Euclidean distance R_l between the BS and the l th scatterer at slow-time index m_s is given by

$$R_l[m_s] \approx R_c[m_s] + [x'_l \cos(\Theta_c[m_s] - \theta_0) - y'_l \sin(\Theta_c[m_s] - \theta_0)] \cos \varphi + z'_l \sin \varphi \quad (6)$$

where (x'_l, y'_l, z'_l) are the local coordinates of scatterer l , θ_0 is the initial target-centroid azimuth angle, and φ is the elevation of the LoS path between the BS and the target center. The translational displacement of the target geometric center is modeled as $R_c[m_s] = R_0 + v_0 m_s T_{\text{SRI}} + \frac{1}{2} a_0 (m_s T_{\text{SRI}})^2$, where v_0 is the initial radial velocity, and $a_0 = (\omega_0 \cos \varphi)^2 R_0$ is the centripetal acceleration induced by the apparent rotation of the target, with $\omega_0 \cos \varphi$ representing the effective angular velocity in the image projection plane (IPP). Moreover, $\Theta_c[m_s] = \Theta_0 + \omega_0 m_s T_{\text{SRI}}$ is the rotation angle, with Θ_0 the initial rotation angle (here equivalent to the target heading direction angle). The effective angular velocity $\omega_0 \cos \varphi$ is assumed constant over the CPI.

Applying the angle-difference identities and a Taylor expansion of $\sin(\omega_0 m_s T_{\text{SRI}})$ and $\cos(\omega_0 m_s T_{\text{SRI}})$ up to second order under the small-rotation over the CPI, i.e., $\omega_0 m_s T_{\text{SRI}} \ll 1$, (6) can be rewritten as

$$R_l[m_s] \approx R_c[m_s] + [x'_l \cos(\Psi_0) - y'_l \sin(\Psi_0)] \cos \varphi + z'_l \sin \varphi + \underbrace{[-x'_l \sin(\Psi_0) - y'_l \cos(\Psi_0)] \omega_0 m_s T_{\text{SRI}} \cos \varphi}_{\Delta R_{\text{walk}}} + \underbrace{[-x'_l \cos(\Psi_0) + y'_l \sin(\Psi_0)] \frac{1}{2} \omega_0^2 (m_s T_{\text{SRI}})^2 \cos \varphi}_{\Delta R_{\text{curv}}} \quad (7)$$

where $\Psi_0 = \Theta_0 - \theta_0$ is the initial aspect angle. From (7), it can be noticed that target rotation generated by the motion leads scatterer l to migrate from its initial range bin due to two range-drift terms, denoted by ΔR_{walk} and ΔR_{curv} and referred to as range walk and range curvature, respectively.⁵

From (7), the Doppler shift term can then be obtained by computing the derivative, as follows

$$f_D[m_s] = \frac{2}{\lambda} \frac{dR_l(t)}{dt} \Big|_{t=m_s T_{\text{SRI}}} = \frac{2}{\lambda} \left[\frac{dR_c(t)}{dt} \Big|_{t=m_s T_{\text{SRI}}} - \underbrace{[x'_l \sin(\Psi_0) + y'_l \cos(\Psi_0)]}_{u} \omega_0 \cos \varphi - [x'_l \cos(\Psi_0) - y'_l \sin(\Psi_0)] \omega_0^2 m_s T_{\text{SRI}} \cos \varphi \right] \quad (8)$$

where the term denoted by u represents the cross-range coordinate associated with scatterer l , while the quadratic Doppler term is responsible for cross-range distortions. However, the latter can be neglected when its amplitude is smaller

⁵It is worth noting that, when the combined effect of ΔR_{walk} and ΔR_{curv} produces a range migration that exceeds the range-resolution cell, the energy of l spreads over multiple range bins and the image becomes defocused. In such cases, range-cell migration correction (RCMC) is required [7].

than the Doppler frequency resolution $\Delta f_D = 1/(M_s T_{\text{SRI}})$ over the entire CPI [14]. The corresponding cross-range resolution is

$$\Delta u = \frac{\lambda}{2\omega_0 \cos \varphi} \Delta f_D. \quad (9)$$

III. IMAGE FORMATION

For IVA range–Doppler image formation, translational motion compensation (TMC) is required to estimate and compensate for the target’s time-varying translational motion parameters. These parameters are represented by the range shift terms $v_0 m_s T_{\text{SRI}}$ and $\frac{1}{2} a_0 (m_s T_{\text{SRI}})^2$ in $R_c[m_s]$, and its derivative given in (8). After compensation, the target range becomes time-invariant, and the Doppler frequencies remain approximately constant over the entire CPI. Specifically, TMC comprises both range alignment and phase adjustment.

A. Range alignment via cross-correlation

The cross-correlation approach for range alignment detailed in [7, Chapter 4] is adopted. Starting from the frequency-domain sensing matrix \mathbf{G}_s in (5), a column-wise FFT is first performed across subcarriers to obtain a matrix \mathbf{F}_s , whose columns correspond to time-reversed range profiles. As a second step, an element-wise modulus operation is applied to \mathbf{F}_s , and an inverse fast Fourier transform (IFFT) is then performed for each matrix column, i.e., OFDM symbol. The reference profile is then selected as the column corresponding to sensing symbol index $(M_s/2) - 1$, and its complex conjugate is multiplied element-wise with each column of \mathbf{F}_s , producing a correlation matrix \mathbf{P}_s . An IFFT across the frequency dimension (i.e., across rows) of \mathbf{P}_s yields the cross-correlation functions, whose peak locations indicate the range shifts (in range-cell units) relative to the reference profile. As a last operation, each range profile of index m_s can be shifted back by the related estimated shift amount $q_{m_s} \in [-K_s/2, (K_s/2) - 1]$.

Each q_{m_s} is then mapped to a phase term as $\Phi_{m_s} = \frac{2\pi}{K_s} q_{m_s}$. A phase unwrapping operation is subsequently applied to remove discontinuities larger than π , obtained by adding appropriate multiples of $\pm 2\pi$ so that adjacent phase differences satisfy $|\bar{\Phi}_{m_s} - \bar{\Phi}_{m_s-1}| < \pi$. The resulting continuous phase term $\bar{\Phi}_{m_s}$ is finally mapped back to range-cell units as $\bar{q}_{m_s} = \frac{K_s}{2\pi} \bar{\Phi}_{m_s}$. Subsequently, a quadratic least-squares fit is performed to regularize the drift, as follows:

$$(\tilde{a}_0, \tilde{a}_1, \tilde{a}_2) = \arg \min_{a_0, a_1, a_2} \sum_{j=1}^{M_s} \left(\bar{q}_j - (a_0 + a_1 j + a_2 j^2) \right)^2 \quad (10)$$

thereby obtaining the range drift $\tilde{q}_{m_s} = (\tilde{a}_0 + \tilde{a}_1 (m_s + 1) + \tilde{a}_2 (m_s + 1)^2)$, with $m_s = 0, \dots, M_s - 1$.

The corresponding delay is then obtained as: $\tau_{m_s} = \tilde{q}_{m_s} \Delta \tau$, where $\Delta \tau = 1/(K_s \Delta f)$ denotes the delay-domain sampling interval, corresponding to the system’s delay resolution.⁶

⁶The relationship between delay resolution and range resolution is given by $\Delta r = c \Delta \tau / 2$.

Lastly, for each sensing sample g_{k, m_s} in (5), delay compensation is applied via a phase ramp across subcarriers k , thus obtaining $\Gamma_{k, m_s} = g_{k, m_s} e^{j 2\pi k \Delta f \tau_{m_s}}$. Given the matrix Γ of elements Γ_{k, m_s} , M_s aligned range profiles $\mathbf{s}_R^{(m_s)} \in \mathbb{C}^{K_p \times 1}$ are then reconstructed by performing a column-wise K_p -point FFT across subcarriers⁷

$$\mathbf{s}_R^{(m_s)} = \text{FFT}_{K_p} \{ \Gamma_{:, m_s} \} \quad (11)$$

where $K_p > K_s$ enables zero-padding in the frequency domain and is chosen as the smallest power of two greater than or equal to $2K_s$.

B. Minimum-variance phase-adjustment method

After range alignment, to remove phase drifts and obtain an approximately linear phase in the range cells occupied by the target, we apply a phase-adjustment procedure based on a minimum-variance criterion [7, Chapter 4]. Specifically, the minimum-variance method selects a small set of range cells whose envelope range profiles exhibit the lowest variance. Using these reference cells, we estimate a symbol-to-symbol phase-correction function, computed across symbols and averaged over the selected range cells, and then apply this correction to all range cells. In particular, the following common phase error (CPE) function needs to be estimated

$$\phi_{\text{CPE}}(m_s) = -\frac{4\pi}{\lambda} [R_0 + v_0 m_s T_{\text{SRI}} + \frac{1}{2} a_0 (m_s T_{\text{SRI}})^2]. \quad (12)$$

Let \mathcal{R} denote the set of n_{ref} range cells (indexes) selected by the minimum-variance criterion. A consistent estimate of the CPE is

$$\hat{\phi}_{\text{CPE}}(m_s) = \frac{1}{n_{\text{ref}}} \sum_{r \in \mathcal{R}} \text{unwrap}(\phi_r(m_s) - \phi_{r_0}(m_s)) + \phi_{r_0}(m_s) \quad (13)$$

where $\phi_r(m_s) = \arg\{\mathbf{s}_R^{(m_s)}[r]\}$ and $r_0 \in \mathcal{R}$ is the first reference cell. The $\text{unwrap}(\cdot)$ operator removes the 2π phase ambiguities as already explained. The phase correction is then applied element-wise to all range cells at time index m_s , as

$$\tilde{s}_R^{(m_s)}[n] = s_R^{(m_s)}[n] e^{-j \hat{\phi}_{\text{CPE}}(m_s)}, \quad n = 0, \dots, K_p - 1. \quad (14)$$

From (14), by fixing the range cell n and moving over the slow-time, we obtain the row vector $\tilde{\mathbf{s}}_R[n]$. Finally, the range-Doppler image is formed by applying an M_p -point FFT to $\tilde{\mathbf{s}}_R[n]$ over the M_s slow-time samples as

$$\mathcal{P}[n, :] = |\text{FFT}_{M_p} \{ \tilde{\mathbf{s}}_R[n] \}|, \quad n = 0, \dots, K_p - 1 \quad (15)$$

where $M_p > M_s$ is here set to the smallest power of two greater than or equal to $10M_s$, and $\mathcal{P}[n, :]$ denotes the n th row of the range-Doppler matrix $\mathcal{P} \in \mathbb{R}^{K_p \times M_p}$, whose columns are indexed by q .

⁷When computing range profiles via FFT, the result is a time-reversed and circularly shifted version of the IFFT-based profile (see, e.g., [11]). A one-bin circular rotation and a left-right flip are thus applied to the resulting profile to correctly position the zero-delay bin and obtain an increasing range axis.

C. Imaging performance metrics

The IC quantifies image focusing and is defined as the normalized standard deviation of the image intensity [7]. Given the IVA image data \mathcal{P} in (15), we compute IC over a region of interest $\tilde{\mathcal{P}} \in \mathbb{R}^{\hat{K}_p \times \hat{M}_p}$ cropped from \mathcal{P} and centered at the ground-truth target-centroid. Precisely, letting μ denote the mean over all elements of $\tilde{\mathcal{P}}$, i.e., $\mu = \frac{1}{\hat{M}_p \hat{K}_p} \mathbf{1}_{\hat{K}_p}^\top \tilde{\mathcal{P}} \mathbf{1}_{\hat{M}_p}$, the constraint is expressed as $\text{IC} = \frac{1}{\mu \sqrt{\hat{M}_p \hat{K}_p}} \|\tilde{\mathcal{P}} - \mu \mathbf{1}_{\hat{K}_p \times \hat{M}_p}\|_F$.

In addition to IC, system performance is also evaluated in terms of target-centroid estimation along the range dimension. The image is first normalized to unit peak, $\tilde{\mathcal{P}}[n, q] = \mathcal{P}[n, q] / \max_{n, q} \mathcal{P}[n, q]$, then we define a threshold

$$\delta = \epsilon \cdot (\mathcal{P}_{\max} - \mathcal{P}_{\min}) \quad (16)$$

where $\mathcal{P}_{\max} = \max_{n, q} \tilde{\mathcal{P}}[n, q]$, $\mathcal{P}_{\min} = \min_{n, q} \tilde{\mathcal{P}}[n, q]$ and $\epsilon \in (0, 1)$ sets the detection threshold as a fraction of the amplitude span. Then, the thresholded image is

$$\tilde{\mathcal{P}}_\delta[n, q] = \begin{cases} \tilde{\mathcal{P}}[n, q], & \text{if } \tilde{\mathcal{P}}[n, q] \geq \delta, \\ 0, & \text{otherwise.} \end{cases} \quad (17)$$

The target-centroid range is finally estimated from $\tilde{\mathcal{P}}_\delta[n, q]$ as the intensity-weighted centroid along the range axis.

IV. NUMERICAL RESULTS

This section analyzes the performance of the proposed monostatic ISAC-IVA setup. For both communication and sensing, the BS transmits 5G NR signals in the upper mid-band using QPSK-modulated symbols, with $f_c = 6.7$ GHz, $\Delta f = 30$ kHz and $K = 13200$ active subcarriers, corresponding to a total bandwidth of around 400 MHz. The OFDM symbol duration and the frame duration are set to $T_s = 35.7$ μ s, and $T_f = 10$ ms, respectively, considering $M = 280$ OFDM symbols per frame. The fraction of active subcarriers for sensing ρ_f is varied from 0.2 to 1, yielding a range resolution that spans from $\Delta r \approx 1.89$ m to $\Delta r \approx 0.38$ m, respectively. For the target, we consider two heading direction angles $\Theta_0 \in \{270^\circ, 300^\circ\}$, measured anticlockwise from the positive x -axis. In this setup, the number of sensing symbols is fixed to $M_s = 220$ for heading $\Theta_0 = 270^\circ$ and $M_s = 200$ for $\Theta_0 = 300^\circ$. Using different M_s values is motivated by the need to keep $\omega_0 \cos \varphi$ approximately constant over the CPI. In both cases, the sensing repetition interval is $T_{\text{SRI}} = 1$ ms, thus reserving only a fraction $\rho_t \simeq 0.036$ of the frame-time resources for sensing. Moreover, $P_T = 30$ dBm, while $N_0 = k_B T_0 F$, with $k_B = 1.38 \cdot 10^{-23}$ J/K the Boltzmann constant, $T_0 = 290$ K, and $F = 5$ dB the noise figure.

The BS is placed at $(x_r, y_r, z_r) = (0, 0, 25)$ m in the global system with two separate ULAs with $N_T = N_R = 10$ elements and azimuthal aperture (i.e., beamwidth) $\Delta \Theta_T = \Delta \Theta_R = 30^\circ$. Following the 3GPP Release 19 specifications [15], the extended vehicular target is modeled with $L = 5$ point scatterers located at the front, rear, roof, left, and right sides, each having a unit, constant RCS, at coordinates $(2.5, 0, 0)$, $(-2.5, 0, 0)$, $(0, 0, 0)$, $(0, 1, 0)$, and $(0, -1, 0)$ m in

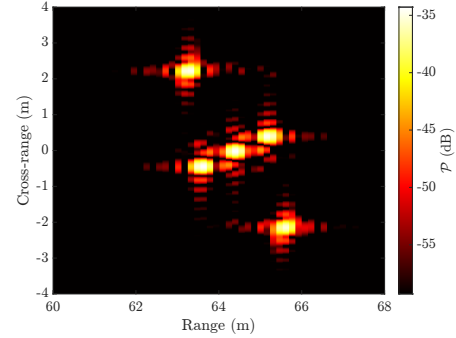


Fig. 2. IVA image (IPP plane) of the vehicle for $v = 30$ m/s and $\rho_f = 1$.

the local (target-fixed) coordinate system. The target center, coinciding with the roof scatterer, is represented in global coordinates with $(x_{t_c}, y_{t_c}, z_{t_c})$, with a fixed height $z_{t_c} = 1.6$ m. Along the target trajectory, for the two considered heading angles Θ_0 , the midpoint-trajectory position is set at $(x_{t_c}, y_{t_c}) = (60, 0)$ m. When $\Theta_0 = 270^\circ$, the coordinate x_{t_c} remains constant throughout the trajectory.

We consider three target speeds, $v \in \{10, 20, 30\}$ m/s. The resulting cross-range resolution Δu , computed according to (9) is, respectively, $\Delta u \approx \{0.81, 0.41, 0.27\}$ m for heading $\Theta_0 = 300^\circ$, and $\Delta u \approx \{0.66, 0.33, 0.22\}$ m for $\Theta_0 = 270^\circ$. The number of reference range cells for phase-adjustment, selected via the minimum-variance criterion of Section III-B, is set to $n_{\text{ref}} = 3$ for $\Theta_0 = 270^\circ$ and $n_{\text{ref}} = 5$ for $\Theta_0 = 300^\circ$, yielding the vehicle image shown in Fig. 2.⁸

Two analyses are conducted: 1) image-quality evaluation based on the IC metric, and 2) assessment of the target-centroid estimation accuracy in the range domain. A total of $N_{\text{MC}} = 1000$ Monte Carlo iterations are performed along the target trajectory. For contrast analysis, \hat{K}_p and \hat{M}_p are chosen to match the dimensions of the image in Fig. 2, and the mean image contrast IC_{mean} is obtained by averaging over N_{MC} iterations with $\Theta_0 = 300^\circ$. In the centroid analysis, accuracy is expressed through the RMSE of the estimated centroid, denoted as RMSE_c , for both Θ_0 values and a threshold of $\epsilon = 0.3$.

A. Image contrast

Fig. 3 shows IC_{mean} versus the fraction of subcarriers allocated to sensing for three target speeds and $\Theta_0 = 300^\circ$. While the cross-range resolution Δu is fixed for a given speed, the range resolution improves with increasing ρ_f , which explains the overall upward trend of the IC_{mean} curves. For $\rho_f \leq 0.3$, the images remain blurred, and the target shape is barely recognizable. When ρ_f equals 0.7, 0.6, and 0.5 at target speeds of 10, 20, and 30 m/s, respectively, the target shape starts to become clearly discernible, with the roof, left, and right point scatterers appearing as distinct features.

⁸Based on the target geometry, trajectory, and sensing parameters M_s and T_{SRI} , the quadratic Doppler term, and the resulting range walk ΔR_{walk} and range curvature ΔR_{curv} , are negligible and do not affect the imaging performance.

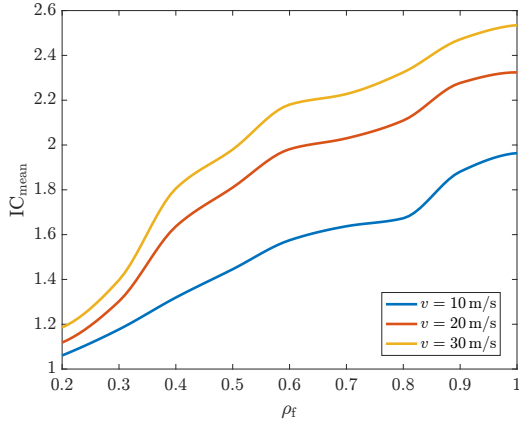


Fig. 3. IC_{mean} of the IVA image for $\Theta_0 = 300^\circ$ as a function of target speed and sensing subcarrier fraction ρ_f .

Beyond these operating points, further increasing ρ_f provides additional image contrast; however, a parsimonious choice of ρ_f preserves bandwidth for communication while still ensuring satisfactory target representation and recognition. Finally, higher target speeds yield larger IC_{mean} values, consistent with the fact that higher translational velocity induces a larger effective angular velocity and thus finer cross-range resolution.

B. RMSE of target-centroid range

Fig. 4 shows the target-centroid range RMSE_c varying the fraction of subcarriers for sensing. For $\Theta_0 = 270^\circ$, RMSE_c decreases rapidly as ρ_f increases, while for $\Theta_0 = 300^\circ$ the reduction is more gradual and starts from larger errors for small ρ_f . This difference arises from the target geometry: at $\Theta_0 = 270^\circ$, the front and rear scatterers are nearly iso-range with the roof point, thus stabilizing the centroid even under coarse range resolution. Contrariwise, this geometric alignment is absent for $\Theta_0 = 300^\circ$. As ρ_f increases and range resolution improves, both trajectories achieve very low errors, with $RMSE_c < 0.1 \text{ m}$ for $\rho_f > 0.8$. Notably, for $\Theta_0 = 270^\circ$, comparable estimation accuracy is already achieved for moderate values of $\rho_f \approx 0.4$, showing that reliable centroid localization can be maintained while preserving bandwidth for communication. At very high ρ_f , the $\Theta_0 = 300^\circ$ case slightly outperforms due to its centroid lying closer to the center of a sampled range bin at the attained resolution. In both cases, target speed (namely cross-range resolution) has only a marginal effect compared with ρ_f variations.

V. CONCLUSION

In this work, an IVA technique for a monostatic ISAC system using a MIMO-OFDM waveform was developed, and its performance was evaluated for a moving extended vehicular target. Range alignment and phase compensation were performed via known cross-correlation and the minimum-variance method. Simulation results show that increasing the sensing subcarrier fraction ρ_f improves image focusing and reduces the target-centroid range estimation error, with the target shape becoming discernible and $RMSE_c < 30 \text{ cm}$ for $\rho_f \geq 0.5$ across

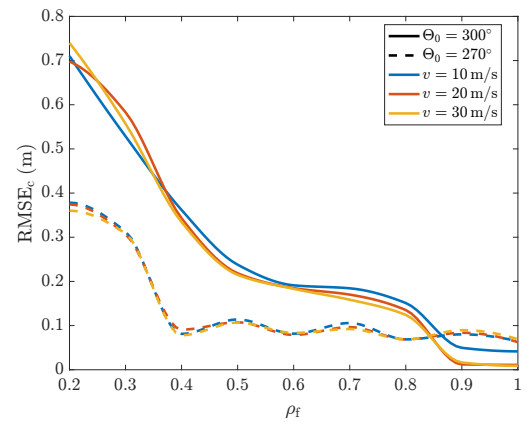


Fig. 4. Target-centroid range estimation error as a function of target speed and sensing subcarrier fraction ρ_f .

both considered trajectories. These findings indicate that good target localization and high-quality imaging can be achieved even with a moderate sensing bandwidth, while using only 3.6% of the frame-time for sensing, enabling an effective trade-off between sensing performance and communication resource utilization.

REFERENCES

- [1] M. Rizzi, M. Manzoni, S. Tebaldini, A. V. Monti-Guarnieri, C. M. Prati, D. Tagliaferri *et al.*, "Multi-beam automotive SAR imaging in urban scenarios," in *Proc. IEEE Radar Conf.*, NY, USA, Mar. 2022.
- [2] M. Manzoni, S. Tebaldini, A. V. Monti-Guarnieri, C. M. Prati, D. Tagliaferri, M. Nicoli *et al.*, "Automotive SAR imaging: potentials, challenges, and performances," *Int. J. of Microwave and Wireless Tech.*, vol. 16, no. 1, p. 3–12, Feb. 2024.
- [3] M. Manzoni, D. Tagliaferri, M. Rizzi, S. Tebaldini, A. V. M. Guarnieri, C. M. Prati *et al.*, "Motion estimation and compensation in automotive MIMO SAR," *IEEE Trans. Intell. Transp. Syst.*, vol. 24, no. 2, pp. 1756–1772, Feb. 2023.
- [4] L. Zhou, S. Gui, L. Li, and Z. Tian, "Bistatic OFDM ISAR imaging method for non-cooperative moving target in ISAC area," in *Proc. IEEE Asia-Pacific Conf. on Ant. and Prop.*, Guangzhou, China, Nov. 2023.
- [5] B. Zheng and F. Liu, "Random signal design for joint communication and SAR imaging towards low-altitude economy," *IEEE Wireless Commun. Lett.*, vol. 13, no. 10, pp. 2662–2666, Oct. 2024.
- [6] S. Gui, Q. Zhang, Z. Li, K. Liu, S. Dang, L. Fan, and Z. Zhao, "Millimeter-wave ISAC-ISAR imaging system for unknown moving target sensing using USRP," *IEEE Sensors J.*, vol. 25, no. 2, pp. 2978–2987, Jan. 2025.
- [7] V. Chen and M. Martorella, *Inverse Synthetic Aperture Radar Imaging: Principles, Algorithms and Applications*. Inst. of Eng. and Tech., 2014.
- [8] B. Friedlander, "On transmit beamforming for MIMO radar," *IEEE Trans. Aerosp. Electron. Syst.*, vol. 48, no. 4, pp. 3376–3388, Oct. 2012.
- [9] H. L. Van Trees, *Optimum array processing: Part IV of detection, estimation, and modulation theory*. John Wiley & Sons, 2002.
- [10] M. A. Richards, *Fundamentals of radar signal processing*. McGraw-Hill, 2005.
- [11] M. Braun, "OFDM radar algorithms in mobile communication networks," Ph.D. dissertation, Karlsruhe Institute of Technology, 2014.
- [12] L. Pucci, L. Arcangeloni, and A. Giorgetti, "Position and velocity estimation accuracy in MIMO-OFDM ISAC networks: A Fisher information analysis," *arXiv preprint arXiv:2507.01743*, 2025. [Online]. Available: <https://arxiv.org/abs/2507.01743>
- [13] F. Berizzi, M. Martorella, and E. Giusti, *Radar Imaging for Maritime Observation*. CRC Press, 2016.
- [14] D. Cataldo, "Monostatic and bistatic radar imaging super-resolution," Ph.D. dissertation, University of Pisa, 2016.
- [15] *Study on channel model for frequencies from 0.5 to 100 GHz*, 3GPP TR 38.901, 6 2025, version 19.0.0 Release 19.